Image Quality Evaluation of Projection- and Depth Dose-Based Approaches to Integrating Proton Radiography Using a Monolithic Scintillator Detector

Irwin Tendler

Department of Radiation Physics, The University of Texas MD Anderson Cancer Center, Houston, TX 77030, USA

Daniel Robertson

Division of Medical Physics, Department of Radiation Oncology, Mayo Clinic Arizona, 5881 E Mayo Blvd, Phoenix, AZ 85054, USA

Chinmay Darne, Rajesh Panthi, Fahed Alsanea

Department of Radiation Physics, The University of Texas MD Anderson Cancer Center, Houston, TX 77030, USA

Charles-Antoine Collins-Fekete

Department of Medical Physics and Biomedical Engineering, University College London, London

Sam Beddar*

abeddar@mdanderson.org

Department of Radiation Physics, The University of Texas MD Anderson Cancer Center, Houston, TX 77030, USA

The Graduate School of Biomedical Sciences, The University of Texas MD Anderson Cancer Center, Houston, TX 77030, USA

*corresponding author

Funding Details / Acknowledgements: The research reported in this publication was supported by the National Cancer Institute/National Institutes of Health under award number P30CA016672 and the Radiation Oncology and Cancer Imaging Program.

Conflict of Interest: The authors have no relevant conflicts of interest to disclose.

Abstract (300 word limit)

The purpose of this study is to compare the image quality of an integrating proton radiography system, composed of a monolithic scintillator and 2 digital cameras, using integral lateral-dose and integral depth-dose image reconstruction techniques. Monte Carlo simulations were used to obtain the energy deposition in a 3D monolithic scintillator detector (30 × 30 × 30 cm^3 poly vinyl toluene organic scintillator) to create radiographs of various phantoms – a slanted aluminum cube for spatial resolution analysis and a Las Vegas phantom for contrast analysis. The light emission of the scintillator was corrected using Birks scintillation model. We compared two integrating proton radiography methods and the expected results from an idealized proton tracking radiography system. Four different image reconstruction methods were utilized in this study: integral scintillation light projected from the beams-eye view, depth-dose based reconstruction methods both with and without optimization, and single particle tracking proton radiography was used for reference data. Results showed that heterogeneity artifact due to medium-interface mismatch was identified from the Las Vegas phantom simulated in air. Spatial resolution was found to be highest for single-event reconstruction. Contrast levels, ranked from best to worst, were found to correspond to particle tracking, optimized depth-dose, depth-dose, and projection-based image reconstructions. The image quality of a monolithic scintillator integrating proton radiography system was sufficient to warrant further exploration. These results show promise for potential clinical use as radiographic techniques for visualizing internal patient anatomy during proton radiotherapy.

Key words: proton imaging, radiography, scintillator, proton CT, reconstruction

1. Introduction

1.1 Proton Radiography

Currently, one of the greatest obstacles preventing clinicians from taking advantage of the full potential of proton therapy (PT) is the inability to accurately convert X-ray CT Hounsfield Units to proton stopping power ratios (SPRs) – variability in SPR leads to increased range uncertainties in PT planning.[1] The standard practice of applying blanket correction factors to account for range uncertainties negatively influences the conformity of dose distribution of PT and unnecessarily increases exposure to normal tissue.[2,3] Proton radiography (PR) is a method that can be used to potentially alleviate PT range uncertainty issues by using radiographs generated via the therapeutic proton beam to more directly and accurately measure patient-specific SPRs.[4]

During radiation treatment, patients can experience macroscopic anatomical changes such as tumor shrinkage/progression, weight gain/loss, etc. Thus, re-evaluation of the SPR throughout the duration of treatment is important to ensuring continued targeted and conformal beam delivery. PR offers a streamlined strategy for obtaining repeat measurements of SPR, an essential step of adaptive treatment planning, with minimal extraneous dose.[5] In addition to reducing SPR uncertainty, PR can be used as a tool for assisting with patient setup.

PR provides a beam's-eye view of the patient in the treatment position without the need of an additional radiation source (the therapy proton source is used to create the image). In turn, target misalignment errors caused by patient movement between the planning and delivery stages of PT can potentially be minimized. Furthermore, PR can feature a lower imaging dose (compared to digitally reconstructed X-ray radiographs) and allows for the ability to capture proton "port films" useful for field verification – a safety feature often used in photon therapy that is only available for proton radiography, not other types of image guidance in proton radiotherapy.[6,7]

1.2 Proton Radiography Detectors

Proton radiography detectors can primarily be categorized into two groups: integrating and single particle tracking detectors. Single particle tracking detectors, otherwise known as proton-tracking systems, employ position-sensitive high-speed detectors placed along both the entrance- and exit-sides of the patient, see Figure 1. These detectors provide high imaging accuracy by tracking individual proton trajectories and measuring their respective energy loss after traversing the patient. The residual energies of each proton are measured using a calorimeter. This data is combined with path length information to determine the water equivalent thickness (WET) along each proton's trajectory.[8] Images are reconstructed by accounting for individual proton energy loss using these various data points. This type of high-fidelity imaging comes at the cost of an increased imaging time, system complexity and financial cost.[9]

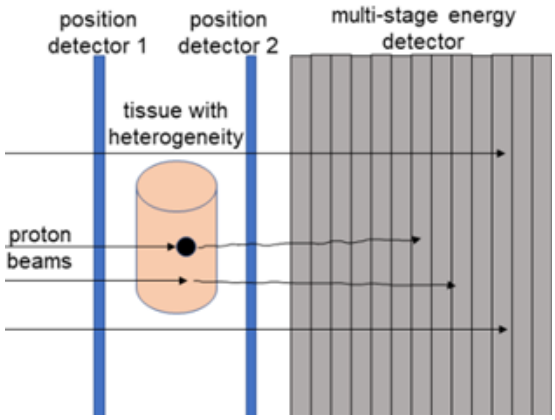

Figure 1: Schematic of a typical proton-tracking system.

Integrating proton radiography systems generate images by integrating the acquired proton fluence using a single detector placed beyond the patient. Proton dose can be integrated via the whole field (passive scattering|) or one spot at a time (pencil beam scanning), and WET values are derived either from integral depth-dose profiles or two-dimensional projections of the proton dose distribution.[10–13] Compared to particle traking, this method requires simpler and less expensive instrumentation: multi-layer ionization chambers or commercial off-the-shelf cameras

can be used instead of high-speed electronics and particle tracking detectors. Additionally, proton-integrating technologies can operate using normal therapeutic beam parameters without the need to modify the beam transport system to achieve ultra-low proton fluence, as is currently required for single particle-tracking detectors.[14] Since a higher dose rate can be used during proton-integrating imaging, acquisition speeds can potentially be quicker versus particle-tracking techniques. Furthermore, because the data from integrating detectors is simpler, image reconstruction is much less computationally intensive, leading to faster image processing (dozens vs. single minutes, proton tracking vs. integrating image processing).[7,15] The drawbacks in this case are a sacrifice in spatial resolution and possibly higher dose exposure to the patient – more protons must be administered as there is less information recorded per proton.[16]

1.3 Integrating Proton Radiography

Two approaches to creating integrating proton radiographs are the beam's-eye-view projection-based and depth dose profile methods. To obtain beam's-eye-view projection, the proton beam is directed, either using passive scattering or spot scanning, into a large solid scintillator block.[10] Scintillation light generated from within the block is captured by a camera facing along the axis of the beam. Individual pixel intensities are then converted to WET metrics by using a calibration look-up table; calibrations factors are obtained by irradiating buildup material of increasing thickness, thereby producing a light intensity vs. WET curve.[11] Image processing steps include: 1) background subtraction 2) median and Gaussian filtering 3) light scattering correction and 4) conversion of pixel intensity to proton range using the previously described look-up table. The advantages of this system – simple instrumentation and large field size imaging – are not without downsides as a lack of integral depth-dose (IDD) data may reduce WET accuracy and proton scatter may contribute to decreased spatial resolution.[10,11,17]

The depth dose-based proton radiography method measures WET values using depth dose curves of individual proton pencil beams (e.g. from a multi-layer ionization chamber, or MLIC) combined with the lateral position of the beam as reported by the integrated spot position monitor in the proton delivery system's nozzle.[18] The initial output from this system may undergo deconvolution or optimization via image processing to improve spatial resolution.[13,19] MLICs are prevalent in many radiation oncology departments allowing for easier adaptation to PR as additional imaging hardware is not required. The drawback of IDD-based PR is that the size of the field that can be imaged by the MLIC is inherently small due to lateral dimensions of the device – numerous images must be obtained using couch shifts.[12]

The objective of this study is to compare the image quality of the projection- and depth dose-based integrating proton radiography techniques. We aim to accomplish this goal through Monte Carlo simulations of a large-volume solid plastic scintillator placed in the beam path using a multi-camera setup. The number of protons chosen for simulation represent a clinically relevant scenario in terms of imparted imaging dose. Contrast-to-noise ratios (CNR) and spatial resolution, established metrics for quantitative image analysis, are used to assess the quality of images resulting from these simulations. Previous work has shown that proton radiography is feasible using a single-camera scintillator imaging system.[20] Potential experimental setups utilizing multiple cameras for imaging of proton beams has also been described.[21] Light emission from a monolithic scintillator placed in the path of the beam is captured in the lateral and beam's-eye-view using 2 digital cameras. This detector setup provides an advantage for our study, as it enables a direct comparison of the projection- and depth dose-based proton radiography methods by simultaneously acquiring both types of data with a single detector. The Monte Carlo data facilitates a comparison between the integrating proton radiography methods and the expected

results from an idealized proton tracking radiography system. In addition to evaluating the image quality of these different proton imaging approaches, we also identify unique imaging artifacts and explore their causes and suggest potential correction methods.

2. Methods

2.1 Monte Carlo Simulation

A Geant4 Monte Carlo software toolkit (version 10.6) was used to simulate clinical proton pencil beams passing through various phantoms; the distribution of energy deposition was obtained by transmitting proton beams through a cubic plastic scintillator.[22] Table 1 provides simulation parameters used during Monte Carlo studies following AAPM TG-268 guidelines.[23] We considered a total of 100 x 100 200-MeV proton pencil beams with virtual source located within a 30 × 30 cm^2 array such that all the beams travelled in parallel towards the phantom – beams were sampled uniformly across the surface of the phantom. Additionally, image artifact studies were conducted using half beam spacing (200 x 200 beams) and double the standard deviation (14.1 mm FWHM). The total number of protons simulated was 1.84 x 10^9; each pencil beam consisted of roughly 7.36 x 10^5 protons and had a spatial structure of $\Delta x = 0.0$ mm, $\Delta y = 0.0$ mm, $\Delta z = 0.0$ mm, and a spread of $\sigma_x = 3$ mm and $\sigma_y = 3$ mm. Figure 2 shows a schematic of the simulation setup. The number of protons chosen for simulation represents a clinically relevant scenario of 2 – 4 mGy per radiograph (considering cross-talk between pencil beams). Therefore, when considering tomographic clinical applications wherein 1 image is acquired per degree of rotation, a dose of approximately 72cGy - 140 cGy is expected. This dose due to imaging is on the high compared to current imaging modalities, however, it is expected that it will be substantially reduced as these imaging techniques discussed in this report are further optimized for clinical implementation.

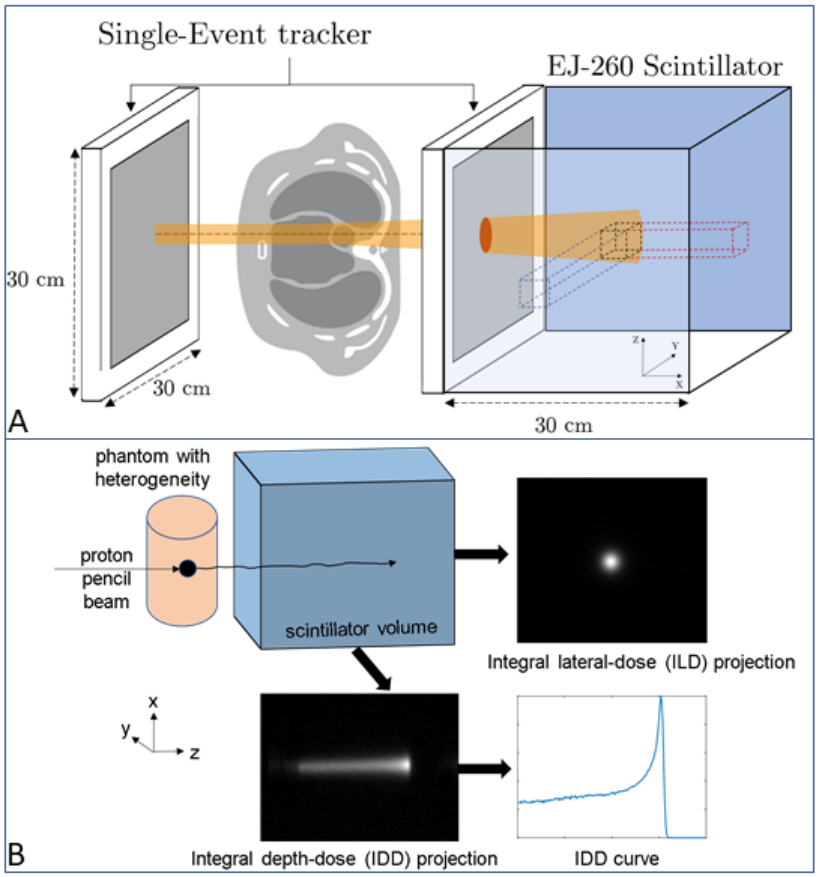

Figure 2: Schematic of the simulation (A) and experimental (B) setup. Dotted blue and red rectangular prisms represent perspectives of the lateral and beam's eye view cameras / detectors in (A).

The simulation included: (i) an aluminum cube (4 x 10 x 10 cm, depth x width x height) placed in a homogeneous water cube of 20 cm side and slanted by 2.5° along the beam axis for spatial resolution analysis and (ii) a "Las Vegas" phantom for contrast analysis. Please note that the two-detector panel setup used in the simulation differs slightly from the experimental setup which utilizes only a single panel. A detailed description of the Las Vegas phantom has been previously given (aluminum square-faced block with 17 holes of varying diameter, 0.5 – 15 mm, and depth 0.5 – 4.5 mm).[24] The proton beam transmitted from the phantom was incident on a 30 × 30 × 30 cm^3 EJ-260 organic scintillator (Eljen Technologies, Sweetwater, Tx) – a green emitting polyvinyl-toluene based scintillator composed of hydrogen (5.21 atoms/cm^3) and carbon (4.70 atoms/cm^3) with a density of 1.023 g/cm^3.The standard electromagnetic (EM) physics model,

emstandard_opt4, was used for high accuracy particle tracking in Geant4[22]. In each simulation setup, the energy deposition and particle-averaged LET were scored for each step individually (energy loss weighted per step length) within a 1 mm^3 grid in the scintillator; results are shown based on the quenched light emission from Birks' law, see equation #1[25]:

$$Equation\ \#1\text{:}\ \frac{dL}{dX} = S\ \frac{\frac{dE}{dX}}{1 + k_B \frac{dE}{dX}}$$

where *dL* is the differential light yield for a differential path *dX* (a step in our simulation), S is the scintillation efficiency set to 1.0 in our simulation, dE/dX represents individual particle LET, k_B is the Birks constant. Recently, a method – open source software package, ExcitonQuenching – for calculating Birks k_B factor for scintillators based on material and physical properties has been published.[26] The EJ-260 (Eljen Technologies, Sweetwater, TX) scintillator block utilized in this study is composed of mainly polyvinyl toluene, yielding a $k_B = 1.59 \times 10^{-2}$ cm/MeV. Since light emission metrics are herein reported in terms of energy, k_B can be used to convert results to light (photon) yield. No light diffraction or parallax effects are accounted for in this simulation and the light yield is projected in parallel from the point of emission until the detection plane.

Table 1: Table outlining parameters utilized for Monte Carlo simulations (following AAPM TG-268 guidelines)[23]

Item Name	Description	References
Code, version/release date	Geant4.10.6.p01	Agostinelly [22]
Validation	ICRU 73 stopping powers incorporated into Geant4 including media such as water. Analysis of Bragg peak position precision, particle dose distributions, and FWHM accuracy are described.	Lechner[27]
Timing	N/A	N/A
Source description	Parallel beam orthogonal to the plane of projection	N/A
Cross-sections	G4HadronElasticPhysics and emstandard_opt4	Lechner[27] and Hall[28]
Transport parameters	MCS based on Lewis theory using the Urban model	Goudsmit[29] and Urban[30]
VRT and/or AEIT	N/A	N/A
Scored quantities	Energy deposition, fluence-averaged LET, and the number of emitted photons	N/A
# histories / statistical uncertainty	$4x10^7$ histories, no uncertainty analysis performed	N/A
Statistical methods	Average light emitted by passively scattered pencil beams considering pencil beam by pencil beam	N/A
Post processing	Fluence-averaged LET was transformed to quenched light using Eq. 1 along the central beam axis	Birks[25]

204 *2.2 Reconstruction Methods*

205 Four different reconstruction methods were utilized in this study: projected scintillation
206 light at the distal camera, depth dose-based reconstruction methods both with and without
207 optimization, and list-mode single-particle tracking proton radiography was used for reference
208 data.[12,13,20] Each of these methods are explained in detail here below.

209 2.2.a List-Mode Single-Particle Tracking Proton Radiography

210 In list-mode proton radiography, energy, position and direction for individual particles is
211 acquired at the front and at the rear tracker. Many radiograph reconstruction methods exist, such
212 as maximum-likelihood reconstruction and binning at depth on the front tracker/rear tracker.[31,32]
213 Each of these methods is associated with unique noise and spatial resolution considerations.[32] For
214 simplicity, simulations in this study, we considered list-mode proton radiography binned at the
215 rear tracker, see Fekete *et. al* for further details.[31,34]

216 2.2.b Projected Scintillation Light Captured at the Distal Camera

217 The distal camera directly captures light emitted from the scintillator, which acts as a
218 surrogate for the total energy deposited in and LET of the medium.[10,11,20] Light captured by the
219 distal camera is converted to WET by using a series of calibration curves generated by irradiating
220 phantoms of various thicknesses, see supplementary material for further explanation.[10,11] This
221 method is expected to provide higher spatial resolution when compared to the below-mentioned
222 lateral reconstruction technique due to the finer gridding of the camera sensor. Unfortunately,
223 however, it may also suffer from comparatively worse contrast due to the inherent properties of
224 energy to range conversion when compared to direct range measurements.[34]

225

226 2.2.c Depth Dose Profile Imaging Without Optimization

227 The lateral (X-Y) and (X-Z) cameras acquire 2-D lateral Bragg peak profiles. The position
228 of the 80% dose point following the Bragg peak maximum is computed for irradiations both with
229 and without a phantom in the beam/scintillator path. The difference between the two traces relates
230 the relative stopping power of the scintillator to a shift in water equivalent thickness experienced
231 by each pencil beam when traversing the phantom. The result of this reconstruction technique
232 produces a coarse map of WET limited in spatial resolution by both the scattering diffusion through
233 the phantom and by the pencil beam grid sampling.

234 2.2.d Depth Dose Profile Imaging with Optimization

235 As mentioned above, lateral images can be used to provide a direct map of WET when
236 combined with reference measurements and beam spot position This is accomplished by
237 accounting for differences in the Bragg peak position generated from irradiations with and without
238 a phantom in the beam path. Depth dose profile imaging can only be employed when recording
239 individual pencil beams, thereby excluding passive scattering systems. Recently, it was.
240 demonstrated that the lateral profile imaging can be used in a reconstruction framework given the
241 right base representation equation.[12,13] Indeed, lateral image reconstruction relies on the fact that
242 the measured Bragg peak profile can be represented by the reference Bragg Peak profile (without
243 phantom) shifted by a convolution of the water equivalent thickness.[12,13] This is expressed in
244 equation #2:

245 $$Equation\ \#2\text{: } \boldsymbol{D_m}(z_i) = \boldsymbol{G}\boldsymbol{D_r}(z_i + \boldsymbol{W})$$

246 Where $\mathbf{D_m}$ represented the value of an individual measured Bragg Peak at depth z_i, **G** is the 2-D
247 Gaussian weighting convolution kernel, **W** is the water equivalent thickness of the projection, and

$\mathbf{D_r}$ is reference measurement Bragg Peak. With such information, one can potentially build minimization algorithm to minimize this equation based on variation in **W**. However, accounting for the normal distribution of the fluence during the convolution process is a non-trivial problem – Eq. 2 does not account for multiple Coulomb scattering since the Gaussian kernel is the same at all depth. Thus, to note, estimating **W** from measurements of $\mathbf{D_m}$ requires the computation of the inverse of **G**, which is non-trivial. Published reports propose using a curvelet minimization method – where curvelets coefficients are minimized in accordance to the above fidelity equation – enacted across an interpolated grid as solution that simultaneously improves spatial resolution and refines gridding.[12,13]

3. Results & Discussion

3.1 Artifact Reduction

Proton radiography conducted under the regime of passive beam scattering irradiation has been previously shown to induce artifacts and image quality deterioration at object-medium interfaces.[10,11] Specifically, images of biological (poultry bone and muscular tissue) and an acrylic cylinder (2 mm thickness) filled with water, demonstrated that pixel intensity values on the side of edge and medium were over- and under-estimated, respectively. Proton radiography simulation images of a Las Vegas phantom undergoing passive scattering irradiation in air are shown in Figure 3. Image formation within the beam's-eye projection process combines both fluence and energy loss information, whereas list-mode events only account for energy loss on a particle by particle basis. Thus, image signal is affected by the scattering effect caused by the phantom on the incident beam. To test this hypothesis, list-mode data was compared to cumulative (fluence and energy loss representing a beam's-eye view projection scenario) and average (only energy loss per particle representing a list-mode radiography scenario) signals, as shown in Figure 3A & 3B. A net

scattering direction on the Las Vegas phantom edge between air and aluminum creates an increased fluence outside the phantom, which in turn leads to an increased signal. However, in the average signal image, this peak disappears since fluence effects are negated. The average relative over- and under-shoot at the edge (symmetrical on both sides of the phantom) was 36% and 52.5%, respectively. Image artifacts were substantially improved by altering the standard deviation and simulation beam spacing. Overshoot at the edge was found to be 22% and 17% for double standard deviation (14.1 mm vs. 7.05 mm FWHM) and half pencil beam spacing (200 x 200 beams vs. 100 x 100 beams), respectively. Undershoot at the edge was found to be 15.4% and 11.6% for double standard deviation and half pencil beam spacing, respectively. It should be noted that this artifact is not visible for slanted edge simulation data (aluminum sheet) because the medium (water) does not provides such a sharp gradient with a lesser scattering (normal distribution of the beam fluence) impact. Quantification and deeper understanding of this artifact is clinically relevant since medium-interface mismatch commonly occurs within the human anatomical structure e.g. nasal cavity in head, lung-chest wall, etc.

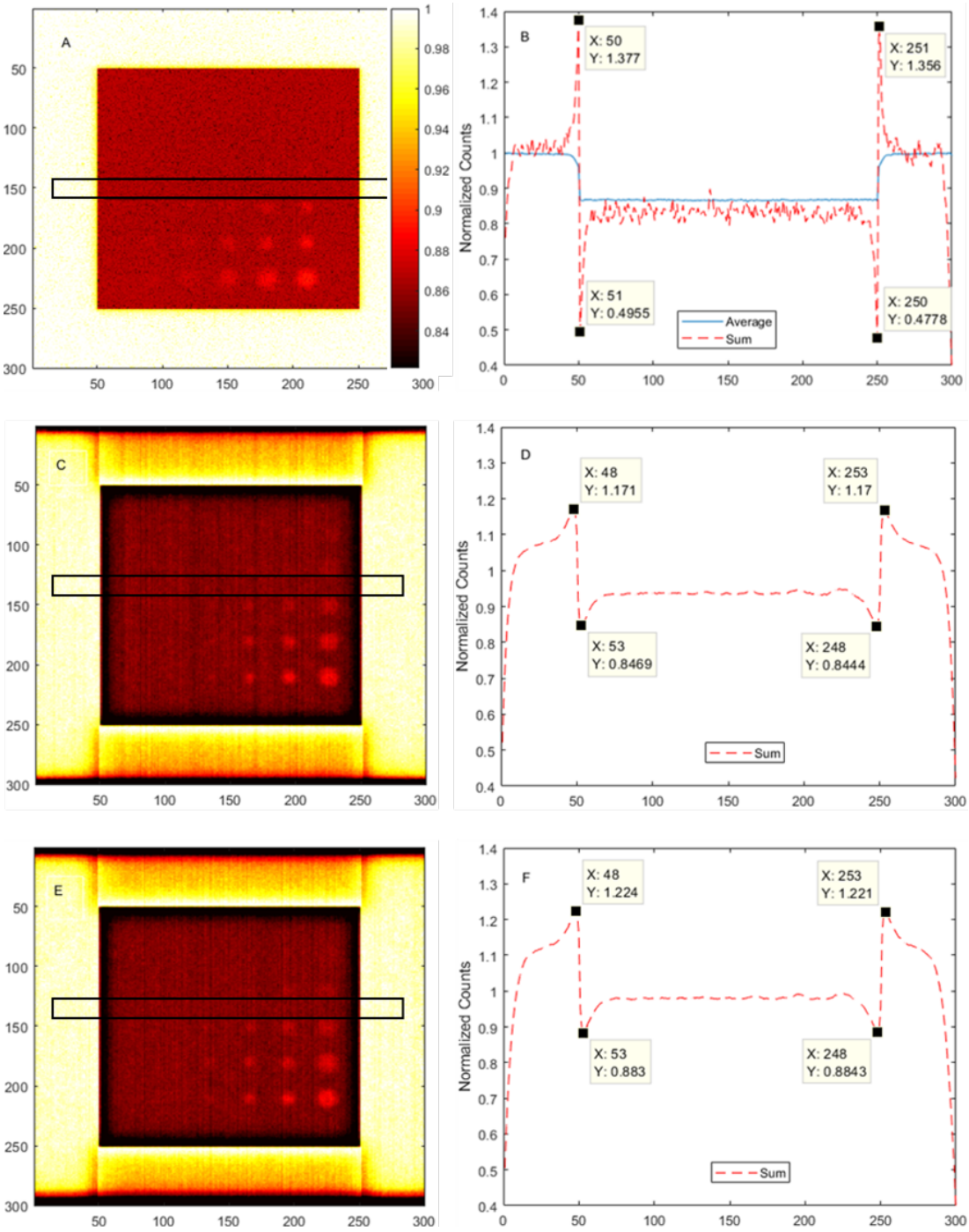

Figure 3: A) Cumulative image of Las Vegas phantom generated using 100 x 100 pencil beams (7.05 mm FWHM) normalized to the maximum intensity pixel value. Black box represents matrix of pixels that were averaged for creating of line profiles. B) Line profiles for average and cumulative (sum) data sets – data is shown normalized to maximum pixel intensity within the average measurements. C) Cumulative image produced using half beam spacing (200 x 200 pencil beams), corresponding summed line profile is shown in D. E) Cumulative image produced using double the standard deviation, 6mm, corresponding line is shown in F. Single colorbar shown in units of normalized counts. Note that counts refers to number of particles emitted in a voxel.

3.2 Spatial Resolution

Spatial resolution was found to be highest for single-event reconstruction, however, its limits could be pushed further since images were recorded at the rear tracker, see Figure 4.[8] It was found that peaks (representing detectable "holes" in the Las Vegas phantom) along the indicated X and Y axis were 2-4, 3-5, 2-3, and 5-5 for DD, DD-opt, BEV, and PTrac reconstruction methods, respectively, see Table 2. Spatial resolution for scintillation light images was lower compared to single-event reconstruction due to scattering through the scintillator. Interfaces in DD and DD-opt are sharper when compared to BEV and PTrac reconstruction methods – slope of line profile is sharper when crossing from hole-aluminum interfaces. This was further shown during imaging of the slanted edge phantom, Figure 4 (FWHM for DD and DD-opt were found to be, on average, 4.5% more sharp and accurate when compared to BEV and PTrac). However, WET values are more accurate in between holes when compared to the other reconstruction methods as is evidenced by stable and flat readings 50 ± 1 mm. In imaging using depth dose profiles without minimization, the spatial resolution is limited by three factors: the pencil beam size, sampling (3mm spread and 3mm distance in this study), as well as the scattering within the phantom. Specifically, when comparing the depth dose (DD) and depth dose-optimized (DD-opt) methods to the beam's-eye view and particle tracking methods, scattering effects in the phantom were identical. However, scattering at the detector were diminished for DD and DD-opt since the dose of many protons is integrated along the plane of the detector. Due to the choices made here, the spatial resolution is particularly strongly limited by the sampling with a Nyquist frequency cutoff (f=1/2a, where a is the sampling rate) of 1.6 lp/cm.

Table 2: Summary of the key findings (CNR, Las Vegas phantom spatial resolution, and FWHM) for each of the reconstruction methods described in this report. * represents poorly defined peaks

Reconstruction Method	CNR	Spatial Resolution (# of discernable Las Vegas holes)	FWHM (# of pixels)
DD	5.1	X = 1 Y = 2	100
DD-opt	77.6	X = 3 Y = 5	103
BEV	83.3	X = 3* Y = 4*	105
PTrac	226.2	X = 5 Y = 5	108

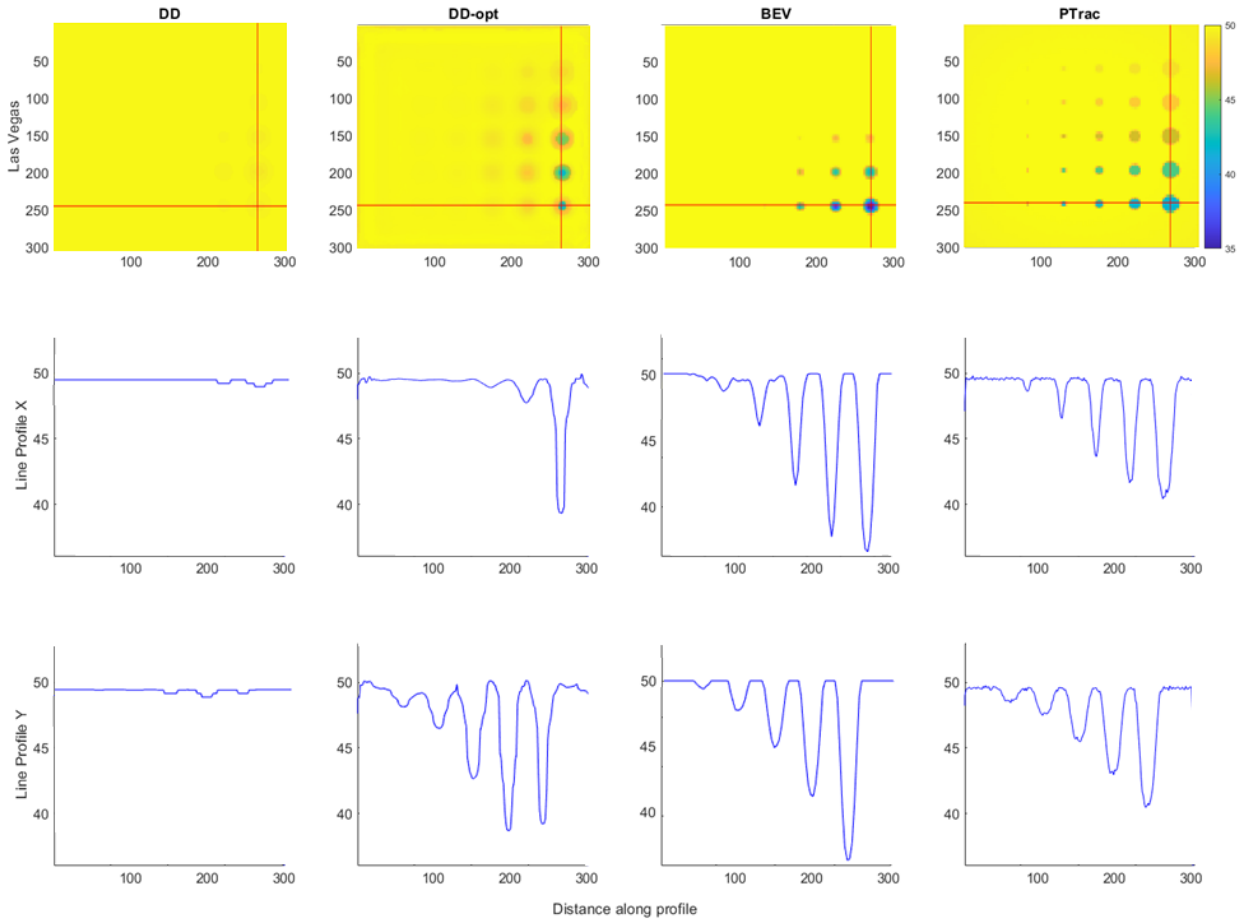

Figure 4: Row 1 shows reconstruction results of depth-dose (DD), depth-dose-optimized (DD-opt), beam's eye view (BEV), and single particle tracking (PTrac) for a Las Vegas phantom. Row 2 and 3 show x and y line profiles respectively. Distance along profile is in units of pixels. Colorbar is shown in units of WET (mm) and is applicable to all Las Vegas phantom images.

A strategy suggesting spatial resolution improvements by interpolating on a finer grid has been published.[12,13] However, this method has no effect on spatial resolution in a conventional phantom (*e.g.* slanted edge and line-pairs) as it does not decompose the Bragg peak signal into well-defined peaks – the sharp edges are poorly represented.[12,13] The methodology presented in reference #13 accounts for the difference between measured and simulated IDDs, both of which have range mixing. Thus, this strategy proposes a method using interpolation within the optimization to generate a thinner image; however, this does not further improve the spatial resolution as demonstrated in this report. This is mostly due to the fact that the optimization algorithm seeks to determine individual shifts in WET corresponding to single differences for each pencil beam. When a reference Bragg peak is split into two Bragg peaks, due to crossing of an interface, this algorithm yields the highest WET of the two. Therefore, in this study, we could not demonstrate any improvement in spatial resolution from this methodology.

Furthermore, experimental data showed reconstructions completed using this methodology were limited by the sampling of the pencil beam. The modulation transfer function (MTF) is a direct measurement of the spatial resolution at different frequencies – it helps us compare the capacity of resolving small features between the different modalities. The MTF range from 0 – 0.1 was shifted for scintillation light signal versus single-event reconstruction, see Figure 6. The scintillation light images had a higher MTF at higher spatial frequencies when compared to single-event reconstructions.

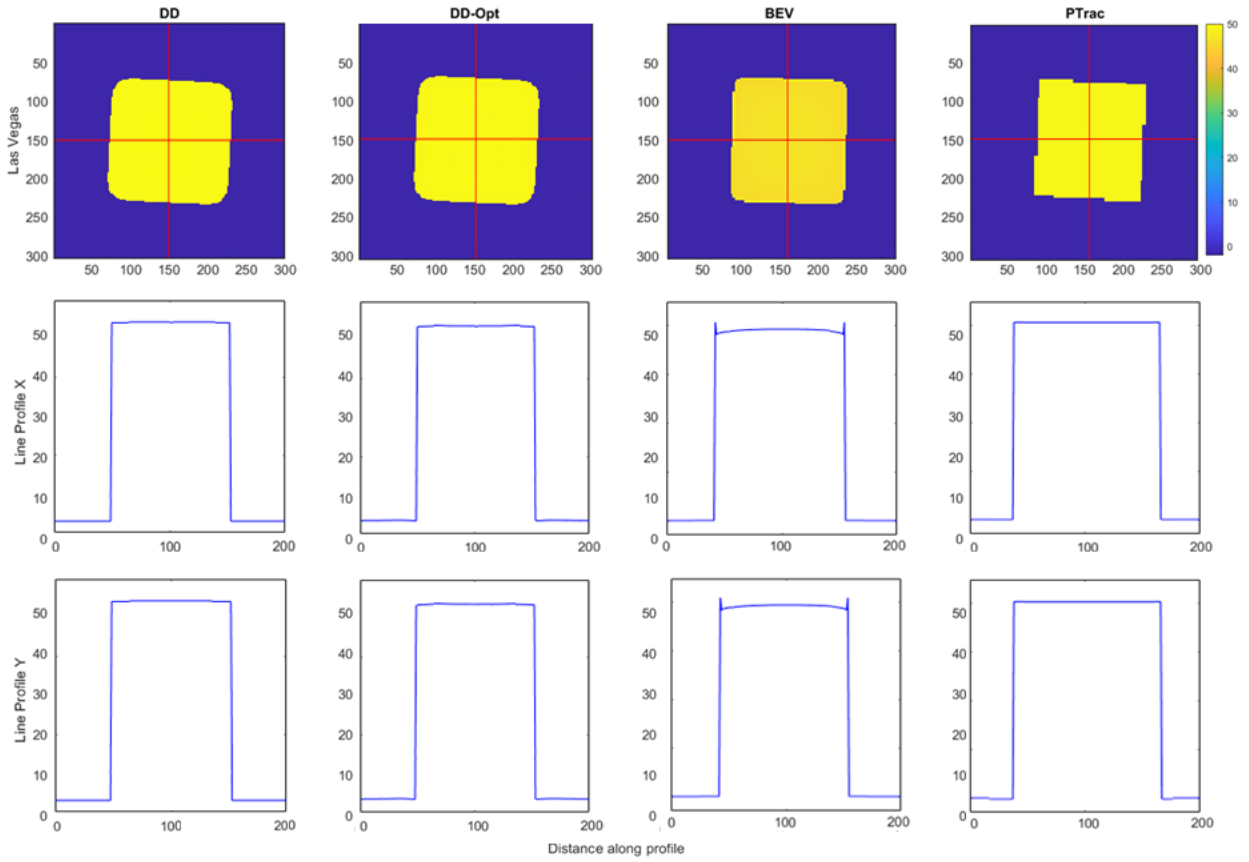

Figure 5: Row 1 shows reconstruction results of depth-dose (DD), depth-dose-optimized (DD-opt), beam's eye view (BEV), and single particle tracking (PTrac) for a slanted edge aluminum phantom. Row 2 and 3 show x and y line profiles respectively. Distance along profile is in units of pixels. Colorbar is shown in units of WET (mm).

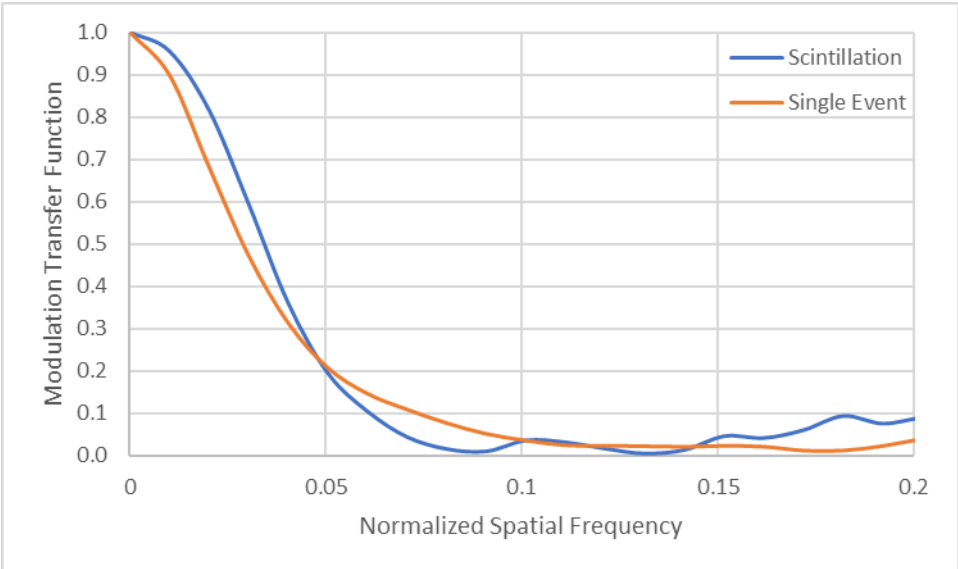

Figure 6: Modulation transfer function versus normalized spatial frequency for scintillation-based images and single event reconstruction. MTF units are line pairs / mm

3.3 Imaging Contrast

Contrast levels (contrast-to-noise ratio, CNR) was measured using Equation 3[35]:

$$Equation\ 3: CNR = \frac{|\mu_{ROI} - \mu_{BKG}|}{\sqrt{{\sigma_{ROI}}^2 + {\sigma_{BKG}}^2}}$$

CNR ranked from best to worst, were found to correspond to single-event WET (CNR = 226.2), depth dose with optimization (CNR = 77.6), depth dose without optimization (CNR = 5.1), and beam's-eye view projection (CNR = 83.3) image reconstructions, see Figure 5. The impact of quenching effects near, or at, the Bragg peak shift should be considered when comparing precision and contrast of the reconstructed signal between scintillation light and Bragg peak shift. This is mainly because scintillation light data is a surrogate for differences in quenching-corrected deposited energy; these results need to be mapped to WET. Bragg peak shift data, on the other hand, account for WET differences by using a scaling factor of the scintillator relative stopping power. It is also important to note that CNR measurements are dependent on the number of simulated protons. Additionally, WET estimation from DD, DD-opt, and BEV are most likely impacted by statistical noise; however, PTrac, which relies on the use of a position tracker is less impacted by statistical noise because several measurements are obtained for a single position, whereas in DD methods, a single image (with noise present) is used for several positions.

3.4 Limitations

Previous work has outlined pros and cons of using large volume scintillators for optical imaging during radiotherapy.[36] Issues related to optical "blurring" can be corrected for by using calibration factors to correct for optically induced artifacts e.g. light scattering. Furthermore, the proton radiography system described in this study may suffers from optical throughput effects such as light leakage in the imaging apparatus (loss of light signal as it passes through the imaging apparatus by means of, for example, imperfect coupling of the lens-intensifier interface); to note,

current simulations do not account for optical-detector induced artifacts.[37] This could potentially be alleviated by attaching an array of CMOS sensors directly to the scintillator via an optically-couple membrane. Inherently, the monolithic scintillator possesses an LET-dependence in terms of effective light response – this can be mitigated by using quenching calibration factors as quenching doesn't significantly affect the calculated beam range (a primary concern in many proton radiography applications). [38]

Each of the detection methodology characterized in this study has a particular set of limitations. For single event imaging, a high spatial resolution is expected, however, it is hard to predict whether any advantage in contrast can be gained. Currently particle rate of detection (~1 – 2 MHz) is not achievable with existing clinical accelerator technology – modern systems lag at about an order of magnitude behind these requirements. Passive scatter imaging requires the shortest acquisition time and can be easily clinically implemented; unfortunately, this type of imaging is associated with the types of artifacts discussed above, as well as those reported in the literature (caused in part by the inherent overlap of beamlets) and is expected to have the lowest expected spatial resolution.[10,11] Pencil beam imaging represents a middle ground, it can be useful in terms of improved image quality, however, it requires a high-speed camera (higher cost) to prevent long imaging time and increased dose to the patient.

The advantages of using Monte Carlo simulations and an ideal detector are multifold: 1) we can use the same perfectly known dataset for each reconstruction method for an accurate comparison without bias and 2) we ignore noise/artefacts related to existing detectors as well as technology limitations to study only the achievable accuracy. Still, this approach compares idealized detector and do not account for varying existing and mentioned limitations (*e.g.* rate constrained single events imaging, optical artefacts in scintillation based integrated imaging) or

new arising methodologies (*e.g.* multi-stage scintillation detector to minimize straggling noise, time-of-flight detector for faster data acquisition). The image quality results should therefore be seen as a best-case scenario, rather than achievable image quality.

4. Conclusion & Future Directions

This study aimed to characterize the image quality of various proton scintillator radiography detection and reconstruction methods. It was determined that the PTrac reconstruction method yielded the best CNR and spatial resolution results when compared to other methods. This method was able to accomplish this without edge artifacts such as those present when using BEV reconstruction methods. Despite having an improved MTF when compared to DD and DD-opt techniques at higher spatial frequencies, the PTrac method had on average 5.8% poorer ability in measuring FWHM versus these two methods. Irrespective of this, we identified PTrac as the best reconstruction methodology in terms of image quality when compared to DD, DD-opt and BEV.

Results discussed above lay the groundwork for future research that will attempt to fully utilize the 2D signal captured by the lateral camera to improve on reconstruction methods previously described.[12,13] In turn, this could potentially reduce the need for utilizing tightly-spaced pencil beam distributions, thereby minimizing dose and acquisition time. Furthermore, the addition of a 3rd lateral-perspective camera could enable 3D methods that would improve radiographic reconstruction accuracy. Presently we use the entire pencil beam to generate a Bragg curve for the depth dose-based reconstruction. If each pencil beam were to be divided into sub-beamlets, an improved spatial resolution could potentially be achieved when compared to the beam's-eye view projection method. Specifically, a 2-D depth-dose profile can provide information regarding material composition when crossed by a pencil beam along the "Y"-axis (assuming the X-axis is the direction of propagation along an X-Y plane). As an exaggerated example: in the case of pencil

beam interacting at the edge of a high gradient block, the top-half of the beam would pass over the edge of the boundary and go further when compared to the bottom half of the beam that would be pulled back. When viewing this scenario in 1-D, one would only see 2 peaks, however, in 2-D, the fraction of the beam that crossed (and did not cross) the block could be identified. Future work will include an evaluation of these image formation methods using measured data from a prototype detector that is currently under development.

5. References

1. Olsen, D. R., Bruland, Ø. S., Frykholm, G. & Norderhaug, I. N. Proton therapy – A systematic review of clinical effectiveness. *Radiother. Oncol.* **83**, 123–132 (2007).

2. Paganetti, H. Range uncertainties in proton therapy and the role of Monte Carlo simulations. *Phys. Med. Biol.* **57**, R99–R117 (2012).

3. Moyers, M. F., Miller, D. W., Bush, D. A. & Slater, J. D. Methodologies and tools for proton beam design for lung tumors. *Int. J. Radiat. Oncol. Biol. Phys.* **49**, 1429–1438 (2001).

4. Schneider, U. & Pedroni, E. Proton radiography as a tool for quality control in proton therapy. *Med. Phys.* **22**, 353–363 (1995).

5. Keall, P., Poulsen, P. & Booth, J. T. See, Think, and Act: Real-Time Adaptive Radiotherapy. *Semin. Radiat. Oncol.* **29**, 228–235 (2019).

6. Seco, J., Dias, M., Depauw, N. & MacDonald, S. SU-E-J-168: Proton Radiography for Pediatric, T-Spine and Lung Malignancies; Development and Enhancement of a Proton Imaging Technique. *Med. Phys.* **38**, 3482–3482 (2011).

7. Prall, M. *et al.* High-energy proton imaging for biomedical applications. *Sci. Rep.* **6**, 27651 (2016).

8. Bashkirov, V. A. *et al.* Novel scintillation detector design and performance for proton radiography and computed tomography. *Med. Phys.* **43**, 664–674 (2016).

9. Poludniowski, G., Allinson, N. M. & Evans, P. M. Proton radiography and tomography with application to proton therapy. *Br. J. Radiol.* **88**, 20150134 (2015).

10. Tanaka, S. *et al.* Development of proton CT imaging system using plastic scintillator and CCD camera. *Phys. Med. Biol.* **61**, 4156–4167 (2016).

11. Tanaka, S. *et al.* Improved proton CT imaging using a bismuth germanium oxide scintillator. *Phys. Med. Biol.* **63**, 035030 (2018).

12. Deffet, S. Proton radiography to reduce range uncertainty in proton therapy. (UCL-Université Catholique de Louvain, 2018).

13. Deffet, S., Farace, P. & Macq, B. Sparse deconvolution of proton radiography data to estimate water equivalent thickness maps. *Med. Phys.* **47**, 509–517 (2020).

14. Johnson, R. P. Review of medical radiography and tomography with proton beams. *Rep. Prog. Phys.* **81**, 016701 (2017).

15. Ordoñez, C. E. *et al.* Fast In Situ Image Reconstruction for Proton Radiography. *J. Radiat. Oncol.* **8**, 185–198 (2019).

16. Zhang, R. *et al.* Improvement of single detector proton radiography by incorporating intensity of time-resolved dose rate functions. *Phys. Med. Biol.* **63**, 015030 (2017).

17. Krah, N., Khellaf, F., Létang, J. M., Rit, S. & Rinaldi, I. A comprehensive theoretical comparison of proton imaging set-ups in terms of spatial resolution. *Phys. Med. Biol.* **63**, 135013 (2018).

18. Farace, P., Righetto, R. & Meijers, A. Pencil beam proton radiography using a multilayer ionization chamber. *Phys. Med. Biol.* **61**, 4078–4087 (2016).

19. Krah, N. *et al.* An advanced image processing method to improve the spatial resolution of ion radiographies. *Phys. Med. Biol.* **60**, 8525–8547 (2015).

20. Darne, C. D. *et al.* A proton imaging system using a volumetric liquid scintillator: a preliminary study. *Biomed. Phys. Eng. Express* **5**, 045032 (2019).

21. Alsanea, F., Darne, C., Robertson, D. & Beddar, S. Ionization quenching correction for a 3D scintillator detector exposed to scanning proton beams. *Phys. Med. Biol.* **65**, 075005 (2020).

22. Agostinelli, S. *et al.* Geant4—a simulation toolkit. *Nucl. Instrum. Methods Phys. Res. Sect. Accel. Spectrometers Detect. Assoc. Equip.* **506**, 250–303 (2003).

23. RECORDS: improved Reporting of montE CarlO RaDiation transport Studies: Report of the AAPM Research Committee Task Group 268 - Sechopoulos - 2018 - Medical Physics - Wiley Online Library. https://aapm.onlinelibrary.wiley.com/doi/full/10.1002/mp.12702.

24. Herman, M. G., Kruse, J. J. & Hagness, C. R. Guide to clinical use of electronic portal imaging. *J. Appl. Clin. Med. Phys.* **1**, 38–57 (2000).

25. Birks, J. *The Theory and Practice of Scintillation Counting*. (Elsevier, 1964). doi:10.1016/C2013-0-01791-4.

26. Christensen, J. B. & Andersen, C. E. Applications of amorphous track structure models for correction of ionization quenching in organic scintillators exposed to ion beams. *Radiat. Meas.* **124**, 158–162 (2019).

27. Lechner, A., Ivanchenko, V. N. & Knobloch, J. Validation of recent Geant4 physics models for application in carbon ion therapy. *Nucl. Instrum. Methods Phys. Res. Sect. B Beam Interact. Mater. At.* **268**, 2343–2354 (2010).

28. Validation of nuclear models in Geant4 using the dose distribution of a 177 MeV proton pencil beam - IOPscience. https://iopscience.iop.org/article/10.1088/0031-9155/61/1/N1.

29. Goudsmit, S. & Saunderson, J. L. Multiple Scattering of Electrons. *Phys. Rev.* **57**, 24–29 (1940).

30. A model for multiple scattering in GEANT4 - CERN Document Server. https://cds.cern.ch/record/1004190.

31. Collins-Fekete, C.-A., Brousmiche, S., Portillo, S. K. N., Beaulieu, L. & Seco, J. A maximum likelihood method for high resolution proton radiography/proton CT. *Phys. Med. Biol.* **61**, 8232–8248 (2016).

32. Volz, L., Collins-Fekete, C.-A., Sølie, J. R. & Seco, J. Theoretical considerations on the spatial resolution limit of single-event particle radiography. *Biomed. Phys. Eng. Express* **6**, 055002 (2020).

33. Alsanea, F. 3D SCINTILLATOR DETECTOR QUENCHING CHARACTERIZATION FOR SCANNING PROTON BEAMS. *Univ. Tex. MD Anderson Cancer Cent. UTHealth Grad. Sch. Biomed. Sci. Diss. Theses Open Access* (2018).

34. Collins-Fekete, C.-A., Dikaios, N., Royle, G. & Evans, P. M. Statistical limitations in proton imaging. *Phys. Med. Biol.* **65**, 085011 (2020).

35. Timischl, F. The contrast-to-noise ratio for image quality evaluation in scanning electron microscopy. *Scanning* **37**, 54–62 (2015).

36. Tendler, I. Quantitative Scintillation Imaging for Dose Verification and Quality Assurance Testing in Radiotherapy. (Dartmouth College, 2020).

37. Robertson, D., Hui, C., Archambault, L., Mohan, R. & Beddar, S. Optical artefact characterization and correction in volumetric scintillation dosimetry. *Phys. Med. Biol.* **59**, 23–42 (2013).

38. Archambault, L. *et al.* Verification of proton range, position, and intensity in IMPT with a 3D liquid scintillator detector system: IMPT verification with 3D liquid scintillator. *Med. Phys.* **39**, 1239–1246 (2012).